Scientific Research Publishing

Open Journal of Fluid Dynamics, 2025, 15(4), 207-221
https://www.scirp.org/journal/ojfd
ISSN Online: 2165-3860
ISSN Print: 2165-3852

CFD Analysis of Pressure and Velocity Profiles in Stenosed Carotid Arteries at Varying Degrees of Occlusion

Lawrence Onyami, Rebecca Muhumuza Nalule*, Fulgensia Kamugisha Mbabazi, Asaph Keikara Muhumuza

Department of Mathematics, Busitema University, Tororo, Uganda
Email: *rnalule.sci@busitema.ac.ug

How to cite this paper: Onyami, L., Nalule, R.M., Mbabazi, F.K. and Muhumuza, A.K. (2025) CFD Analysis of Pressure and Velocity Profiles in Stenosed Carotid Arteries at Varying Degrees of Occlusion. *Open Journal of Fluid Dynamics*, **15**, 207-221.
https://doi.org/10.4236/ojfd.2025.154012

Received: August 18, 2025
Accepted: November 14, 2025
Published: November 17, 2025

Abstract

Cardiovascular diseases remain the leading cause of death globally, with carotid artery stenosis is a major contributor to the global burden of a significant role in ischemic stroke incidence. This study employed Computational Fluid Dynamics (CFD) to analyse pressure, velocity, and wall shear stress (WSS) profiles in carotid stress arteries under three stenosis severities 50%, 70% and 90%. Using COMSOL Multiphysics and the Finite Element method (FEM), simulations were conducted on a two-dimensional artery model, incorating buoyancy forces and energy equations to better reflect hemodynamic behavior. The results demonstrated that as stenosis severity increases, there is a nonlinear rise in peak velocity and pressure drop, accompanied by elevated and more localised WSS at the throat of stenosis. At 90%, stenosis, critical hemodynamic conditions were observed, including excessive WSS (>30 Pa), steep pressure gradients, and downstream flow disturbances. These factors are known contributors to endothelial injury, plaque rupture, and thrombus formation. Additionally, recirculation zones with near zero WSS downstream posed risks for stagnation and atherogenesis. This study highlights CFD as a powerful, non-invasive tool for assessing stroke risk and guiding clinical decision-making. The findings highlight the need for early diagnosis and hemodynamic profiling in managing carotid artery disease, especially in resource limited settings where advanced imaging may be inaccessible.

Keywords

Computational Fluid Dynamics, Carotid Artery Stenosis, Hemodynamics, Pressure Distribution, Velocity Profile

1. Introduction

Hemodynamic determinants of atherosclerosis localization—including low and oscillatory wall shear stress (WSS), flow separation, and recirculation—have long been recognized [1] [2]. Beyond macroscopic correlations, endothelial gene regulation by shear stress (e.g., endothelin-1 suppression) provides a mechanistic link between local hemodynamics and vascular remodeling [3]. From a population perspective, the burden and urgency of improving cardiovascular prevention and diagnosis are well documented [4].

Cardiovascular diseases (CVDs) remain the leading cause of mortality worldwide, accounting for approximately 17.9 million deaths annually and representing 32% of all global deaths [5]. Stroke, one of the most disabling consequences of CVDs, disproportionately affects low- and middle-income countries where diagnostic and treatment resources are limited [6]. The carotid arteries, which supply oxygenated blood to the brain, are highly susceptible to atherosclerotic plaque buildup that progressively narrows the lumen, a condition known as stenosis [7].

As stenosis advances, blood flow experiences substantial hemodynamic alterations, including increased velocity at the narrowed region, steep pressure gradients, and significant changes in wall shear stress (WSS). These disturbances can trigger endothelial injury, plaque rupture, and thrombosis, ultimately leading to ischemic stroke [8]. Specifically, low WSS in post-stenotic regions has been linked to endothelial dysfunction and atherogenesis [9], while elevated WSS within the stenotic segment accelerates plaque destabilization and rupture [10].

Traditional imaging modalities such as Doppler ultrasound, CT angiography, and MRI provide valuable anatomical and flow velocity data but cannot adequately capture complex spatiotemporal flow patterns, especially in high-grade stenosis [11]. In contrast, Computational Fluid Dynamics (CFD) solves the Navier-Stokes equations under physiologically realistic boundary conditions, allowing detailed, non-invasive hemodynamic analysis [12]. This approach has proven increasingly important in stroke risk assessment, surgical planning, and cardiovascular device evaluation, with growing application in patient-specific modeling [13].

Recent studies have advanced CFD capabilities by incorporating pulsatile flow, non-Newtonian blood rheology, vessel wall elasticity, and even thermal and buoyancy effects to better replicate realistic physiological conditions [14] [15]. For instance, Gallo *et al.* [8] highlighted the mechanistic role of WSS in plaque progression, while Liu *et al.* [7] demonstrated that increasing stenosis severity leads to nonlinear rises in velocity and pressure gradients, key factors in stroke risk.

Despite these advancements, few investigations have explored the combined effects of buoyancy forces and energy transport in stenosed arteries, even though evidence suggests that these parameters influence flow stability under pathological conditions [16]. Employing the Boussinesq approximation for buoyancy-driven flows offers a thermodynamically consistent framework for modeling such phenomena [17].

Moreover, the Finite Element Method (FEM), implemented in platforms such as COMSOL Multiphysics, has enabled high-fidelity simulations to capture complex hemodynamics, including flow separation, WSS distribution, and pressure gradients—factors critical to predicting stroke risk and guiding therapeutic interventions [18] [19].

Motivated by these gaps, this study employs CFD simulations to analyze pressure and velocity profiles in carotid arteries with stenosis severities of 50%, 70%, and 90%. A modified incompressible Navier-Stokes model incorporating buoyancy forces and energy equations is applied to 1) characterize hemodynamic alterations across stenosis severities, 2) identify flow conditions associated with thrombosis and plaque instability, and 3) provide insights for improving diagnostic and treatment strategies in resource-limited clinical settings.

2. Materials and Methods

Unlike simplified clinical indices such as Bernoulli-derived gradients, CFD enables high-fidelity quantification of velocity and WSS distributions under complex flow conditions [20]. This section presents the computational modeling approach used to investigate hemodynamic variations in carotid arteries with different stenosis severities. The simulations were conducted in COMSOL Multiphysics 6.1 using the FEM for solving the governing equations of fluid flow and energy transport.

As summarized in **Table 1**, all variables, parameters, and their physical units used in the governing equations are clearly defined for reference throughout the manuscript.

2.1. Research Design

The study was structured in three phases. First, a two-dimensional geometric model of a carotid artery with 50%, 70%, and 90% stenosis was constructed. Second, the governing equations describing blood flow and energy transfer were formulated and discretized. Finally, numerical simulations were carried out to compute velocity, pressure, and WSS distributions at each stenosis level for comparison and interpretation.

2.2. Data Collection and Preparation

Qualitative data on carotid artery stenosis from and related studies were reviewed to understand the hemodynamic properties of blood flow. The mathematical model developed by [16] was subsequently modified to incorporate buoyancy forces and the energy equation. These modifications aimed to evaluate the role of buoyancy in pressure distribution before, within, and after the stenosed region, as well as its impact on flow dynamics, including velocity profiles, acceleration, and deceleration of blood through the constriction factors that potentially contribute to turbulence generation.

Moreover, WSS exerted on the arterial walls was regulated to minimize further

endothelial damage and plaque formation. Simultaneously, secondary flows were considered to facilitate the removal of waste products from the vessel walls, improve nutrient distribution, and reduce hemodynamic resistance. These effects collectively contribute to lowering the cardiac workload and enhancing overall circulatory efficiency.

The energy equation was employed to analyze pressure drops, velocity changes, and flow rates, recognizing that energy transformation in blood flow adheres to Bernoulli's principle (BP). Additionally, energy losses due to viscous dissipation were quantified. Following these modifications, CFD simulations were implemented to discretize and numerically solve the model.

2.3. Geometrical Model and Stenosis Configurations

The internal and external factors that cause stenosis and determine the location of rapture were exposed by the geometry. The schematic diagram was obtained from international conference on Advances in computing and communications [16]. The geometry is sampled to be of 1 mm diameter and total length of 8 mm. Inlet length before stenosed junction is 2 mm and junction is 0.5 mm length while after the junction is 5.5 mm as shown in **Figure 1**.

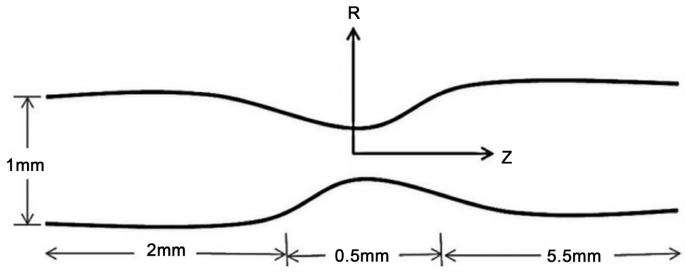

Figure 1. Schematic diagram of a stenosed artery. Source: [22].

Meshing was done on the entire outer and inner surface of the artery. The artery considered is the normal human healthy vein of 6 - 8 mm diameter (**Figure 2**).

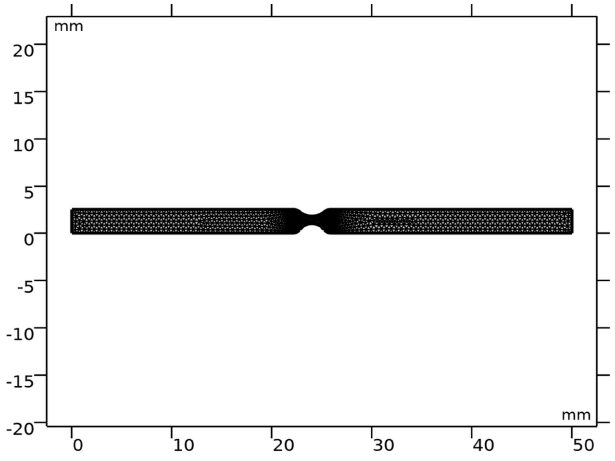

Figure 2. Schematic diagram of a stenosed artery.

2.4. Assumptions

Although blood is a *non-Newtonian*, *shear-thinning* (*rheofluidifying*) *fluid*, numerous studies [14] [21] have shown that in *large arteries* like the carotid, under *high shear rates* and *pulsatile flow conditions*, the *Newtonian assumption* introduces negligible errors in velocity and pressure predictions. Therefore, in this study, blood was modeled as an *incompressible*, *Newtonian fluid* to reduce computational complexity while maintaining acceptable accuracy for hemodynamic assessment. In addition, the flow was considered laminar and pulsatile with physiologically realistic inlet waveforms, vessel walls were treated as rigid to focus on the impact of stenosis severity rather than wall elasticity, and thermal buoyancy effects were incorporated using the Boussinesq approximation to explore their possible influence on flow stability. These simplifying assumptions are widely adopted in hemodynamic simulations of large vessels, though they represent limitations to be addressed in future work.

2.5. Nomenclature

Table 1. Nomenclature of variables and parameters.

Symbol	Description	Unit
u, v	Velocity components in x- and y-directions	m/s
p	Pressure field	Pa
ρ	Density of blood	kg/m^3
μ	Dynamic viscosity of blood	Pa·s
Q	Volumetric flow rate	m^3/s
V_b	Volume of displaced blood	m^3
F_b	Buoyancy force	N
g	Gravitational acceleration	m/s^2
T	Temperature field	K
T_0	Reference temperature	K
k	Thermal conductivity	W/(m·K)
K	Thermal diffusivity	m^2/s
β	Thermal expansion coefficient	1/K
Re	Reynolds number	–
Ra	Rayleigh number	–
ω_1	Fundamental frequency at rest	Hz
ω_2	Fundamental frequency at exercise	Hz
A	Cross-sectional area of the artery	m^2
L	Length scale (artery length)	m
WSS	Wall shear stress	Pa
∇	Gradient operator	–
$\nabla\cdot$	Divergence operator	–
∇^2	Laplacian operator	–

2.6. Derivation of the Governing Equation

The mathematical modeling of blood flow is governed by the conservation of mass, conservation of momentum and conservation of energy equations that control the flow and pressure distribution. Therefore, the mathematical equations governing the conservation laws were controlled by the following parameters and variables.

The inlet boundary conditions were prescribed on the section upstream of the stenosed region, where a specified blood volume entered with defined velocity and temperature profiles. These conditions accounted for both resting and exercise states, with the fundamental frequencies set to $\omega_1 = 1.165$ Hz at rest and $\omega_2 = 2.222$ Hz during exercise. At the outlet, pressure conditions were imposed downstream of the stenosis while maintaining physiologically realistic WSS distributions. Both Dirichlet and Neumann boundary conditions were applied appropriately to govern velocity fields and ensure mathematical well-posedness. The simulations also incorporated blood flow volume quantification, assumed healthy and undamaged carotid arteries, and normal cardiac function to reflect physiological conditions accurately.

Roy *et al.* [22] investigated blood flow in arterial stenoses of varying severities; however, their analysis did not account for buoyancy effects in the distribution of pressure, velocity, and WSS. In contrast, the present study incorporates buoyancy forces into the mathematical model to provide a more physiologically realistic representation of hemodynamics across different stenosis severities.

The 2D Navier-Stokes incompressible modified equations of Laminar pulsatile flow are:

2.7. Governing Equations

The incompressible Navier-Stokes equations, coupled with the continuity and energy equations, governed the flow:

Equation for mass conservation of blood

$$\nabla \cdot \mathbf{u} = 0. \tag{1}$$

The equation for the conservation of momentum

$$\rho \frac{\partial u}{\partial t} + u \cdot \nabla u = -\nabla p + \mu \nabla^2 u \quad \left(\text{momentum equation}\right) \tag{2}$$

$$\rho\left(u\frac{\partial u}{\partial x} + v\frac{\partial v}{\partial y}\right) = -\frac{\partial p}{\partial x} + \mu\frac{\partial^2 v}{\partial y^2} + F_b \tag{3}$$

$$u\frac{\partial u}{\partial x} + v\frac{\partial v}{\partial y} = \frac{-1}{\rho_b}\frac{\partial p}{\partial x} + \frac{\mu}{\rho_b}\frac{\partial^2 v}{\partial y^2} + gV_b \tag{4}$$

where F_b in Equation (3) is the Buoyancy force $= -\rho g V_b$. The negative shows that the force is acting upwards opposing gravity.

Substituting for F_b in Equation (4) and dividing by ρ, we have

$$u\frac{\partial u}{\partial x} + v\frac{\partial v}{\partial y} = \frac{-1}{\rho_b}\frac{\partial p}{\partial x} + \frac{\mu}{\rho_b}\frac{\partial^2 v}{\partial y^2} + gV_b \tag{5}$$

2.8. Measurement of the Volume of Blood V_b

From the definition of volumetric flow rate (Q), which is the volume of fluid passing through a surface per unit time is given by

$$Q = AV_{vb} \tag{6}$$

Obtaining the relationship between Buoyancy F_b and Volumetric flow rate Q Using Archimedes Principal, we have

Upthrust force F_b = Weight of fluid displaced

$$\rho g V_b = Q\rho gt \tag{7}$$

$$V_b = Qt, \text{ substituting for } Q \text{ we obtain,} \tag{8}$$

$$V_b = AV_{vb}t \tag{9}$$

(5) in (8)

$$u\frac{\partial u}{\partial x} + v\frac{\partial v}{\partial y} = \frac{-1}{\rho_b}\frac{\partial p}{\partial x} + \frac{\mu}{\rho_b}\frac{\partial^2 v}{\partial y^2} + gAV_{vb}t \tag{10}$$

2.9. The Principle of Boussinesq Approximation

The Boussinesq approximation (BA) is a simplification of the Navier-Stokes equations widely employed in the analysis of buoyancy-driven flows. It assumes an incompressible fluid and, in the context of blood flow through a stenosed artery, significantly reduces the complexity of the governing equations [23]. By approximating density variations only where they influence buoyancy, BA enables accurate prediction of flow patterns, facilitating the study of pressure-driven hemodynamics in stenotic regions. The pressure gradient across the stenosis induces velocity gradients, which in turn generate WSS that may contribute to arterial wall damage and the formation of atherosclerotic plaques [24]. Hence, employing the Boussinesq approximation simplifies the mathematical treatment of blood flow in stenosed arteries, providing valuable insights for clinicians and aiding in the development of improved cardiovascular interventions.

2.10. Applying the Boussinesq Principle for Buoyancy Driven Flows, to Fully Manage the Flow

Dimensionless Form of the Governing Equations

To simplify the analysis and reduce the number of independent parameters, the governing equations were expressed in dimensionless form using the following scaling relations:

$$x^* = \frac{x}{L},\ y^* = \frac{y}{L},\ u^* = \frac{u}{U_0},\ v^* = \frac{v}{U_0},\ p^* = \frac{p}{\rho U_0^2},\ t^* = \frac{tU_0}{L},\ \theta = \frac{T - T_0}{\Delta T},$$

where L is the characteristic length (e.g., artery diameter), U_0 is the inlet velocity scale, ΔT is the characteristic temperature difference, and ρ is the fluid density.

Using these scales, the two-dimensional incompressible Navier-Stokes and energy equations become

$$\frac{\partial u^*}{\partial x^*}+\frac{\partial v^*}{\partial y^*}=0,$$

$$\frac{\partial u^*}{\partial t^*}+u^*\frac{\partial u^*}{\partial x^*}+v^*\frac{\partial u^*}{\partial y^*}=-\frac{\partial p^*}{\partial x^*}+\frac{1}{Re}\left(\frac{\partial^2 u^*}{\partial x^{*2}}+\frac{\partial^2 u^*}{\partial y^{*2}}\right)+Ra\theta,$$

$$\frac{\partial v^*}{\partial t^*}+u^*\frac{\partial v^*}{\partial x^*}+v^*\frac{\partial v^*}{\partial y^*}=-\frac{\partial p^*}{\partial y^*}+\frac{1}{Re}\left(\frac{\partial^2 v^*}{\partial x^{*2}}+\frac{\partial^2 v^*}{\partial y^{*2}}\right),$$

$$\frac{\partial \theta}{\partial t^*}+u^*\frac{\partial \theta}{\partial x^*}+v^*\frac{\partial \theta}{\partial y^*}=\frac{1}{RePr}\left(\frac{\partial^2 \theta}{\partial x^{*2}}+\frac{\partial^2 \theta}{\partial y^{*2}}\right),$$

where the dimensionless numbers are defined as

$$Re=\frac{\rho U_0 L}{\mu},\quad Pr=\frac{\mu c_p}{k},\quad Ra=\frac{g\beta\Delta TL^3}{\nu\alpha}.$$

Here, Re is the Reynolds number, Pr is the Prandtl number, and Ra is the Rayleigh number representing the influence of buoyancy forces.

The volumetric flow rate is given by.

$$Q=\frac{g\beta\Delta TL^3}{K_\mu Re}=\frac{g\beta L^3\left(T-T_o\right)}{K_\mu Re} \tag{11}$$

Substituting Q into Equation (6), the conservation of momentum equation, we have,

$$u\frac{\partial u}{\partial x}+v\frac{\partial v}{\partial y}=-\frac{1}{\rho_b}\frac{\partial p}{\partial x}+\frac{\mu}{\rho_b}\frac{\partial^2 v}{\partial y^2}+\frac{g\beta L^3\left(T-T_o\right)}{\rho_b K_\mu Re} \tag{12}$$

2.11. The Equation for the Conservation of Energy

$$\frac{\partial T}{\partial t}+u\cdot\nabla T=K\nabla^2 T \tag{13}$$

$$u\frac{\partial T}{\partial x}+v\frac{\partial T}{\partial y}=k\frac{\partial^2 T}{\partial y^2} \tag{14}$$

2.12. Numerical Simulation

Using SpaceClaim, the geometry was designed in cylindrical form and then imported to COMSOL Multiphyscs software where the initial and boundary conditions are fed in. Thereafter, the simulations are run.

2.13. Initial and Boundary Conditions

Density of blood, ρ is 1.05 g·cm^3 (incompressible fluid), viscosity, μ is 0.04 poise (Newtonian fluid), Specific inlet velocity of fluid (blood) was 0.1 m·s^{-1}, pressure at rest and exercise condition were 1.166 H·Z and 2.222 H·Z respectively (Dirichlet boundary condition), no slip at the vessel wall (No relative velocity at the walls), negligible surface tension (Expansion of the vessel is ignored).

3. Results and Discussion

This section presents pressure, velocity, and WSS outcomes for 50%, 70%, and 90% stenosis. To improve readability and facilitate comparison, we summarize key metrics in tables and use multi-panel figures to juxtapose severities on consistent axes and color scales. Table 1 provides a concise summary of the model parameters and symbols employed in the hemodynamic analysis for clarity when interpreting the results.

3.1. Pressure Distribution

Table 2 reports representative pressures upstream, at the throat, and downstream, while Figure 3 shows the spatial pressure fields at each stenosis level. Figure 4 aggregates axial pressure profiles for direct comparison. Values illustrate the nonlinear growth of pressure drop with severity.

Table 2. Summary of pressure at different stenosis levels.

Stenosis	Upstream (Pa)	Throat (Pa)	Downstream (Pa)
50%	800	650	600
%	4000	1200	800
%	30,000	5000	0 - 5000

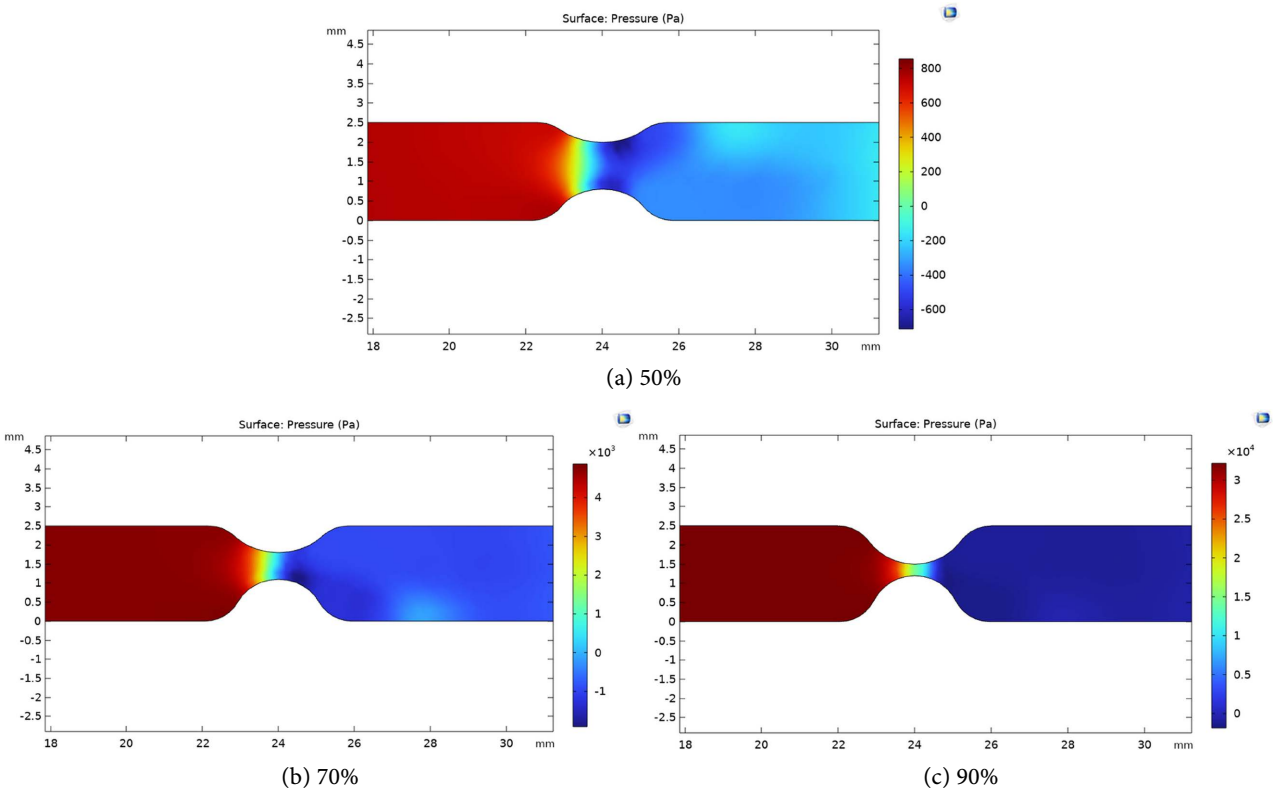

(a) 50%

(b) 70%

(c) 90%

Figure 3. Static pressure distribution for (a) 50%, (b) 70%, and (c) 90% stenosis with a unified color bar.

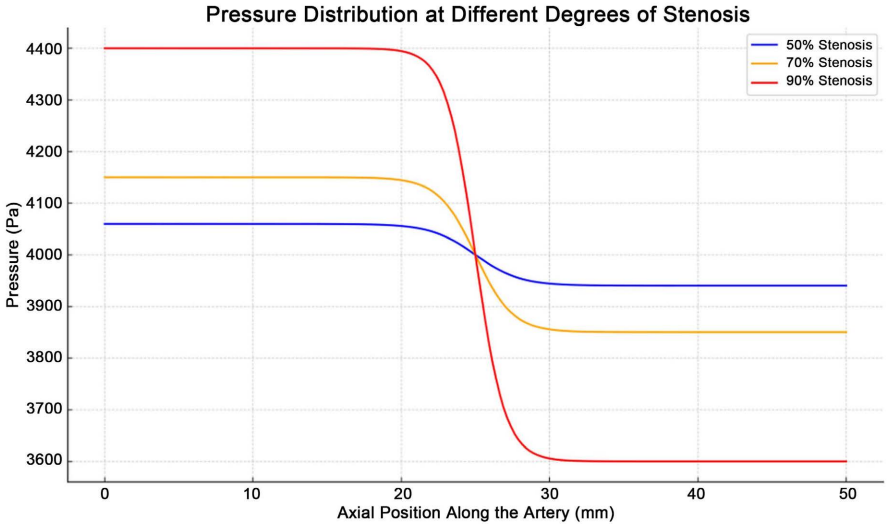

Figure 4. Axial pressure profiles across stenosis severities.

Discussion. Progressive narrowing leads to a steepening pressure drop across the throat and diminished downstream recovery. The pressure drop increases nonlinearly with severity, reflecting jet acceleration and viscous losses in the post-stenotic region. The large upstream head at 90% indicates critical hemodynamic compromise and increased cardiac after load.

3.2. Velocity Profiles

Table 3 summarizes peak velocities; Figure 5 shows a representative velocity magnitude field; Figure 6 overlays axial profiles for all severities.

Table 3. Peak velocities at sampling locations.

Stenosis	Upstream (m/s)	Throat (m/s)	Downstream (m/s)
50%	0.6	1.8	0.9
%	0.8	2.6	1.2
%	1.0	3.6	1.4

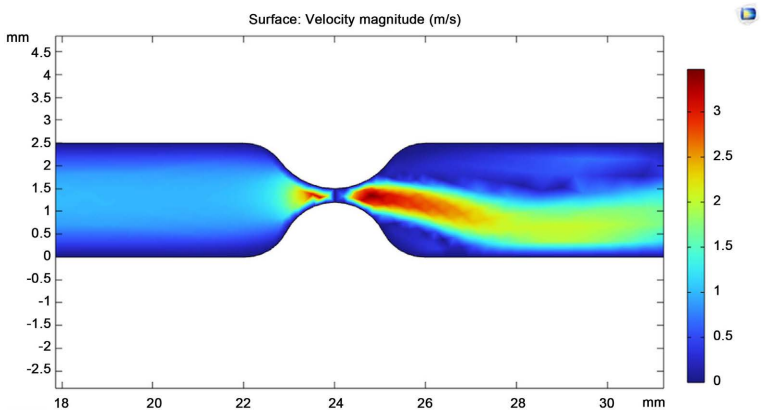

Figure 5. Representative velocity magnitude.

A high-speed jet forms at the throat; post-stenotic disturbances increase with severity (see Figure 6).

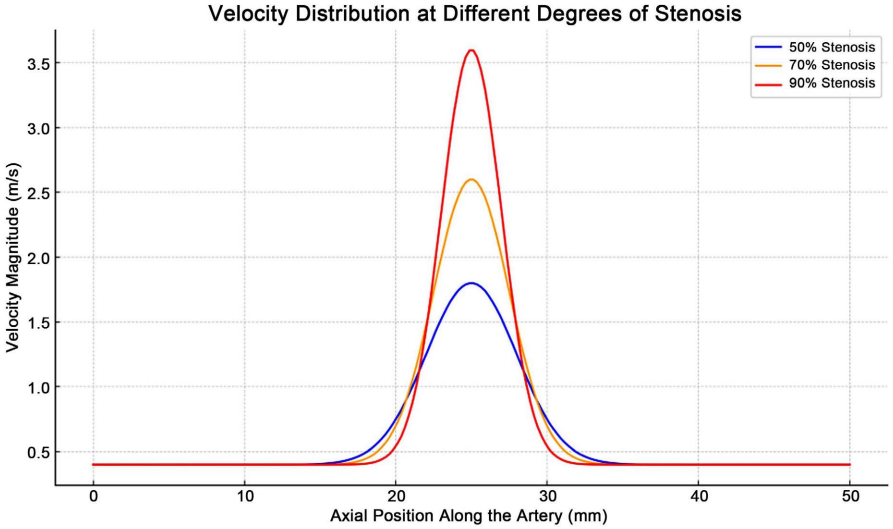

Figure 6. Axial velocity profiles for 50%, 70%, and 90% stenosis.

Discussion. Peak jet velocity scales with severity; recirculation develops downstream at Peak jet velocity rises with stenosis grade, while downstream regions exhibit growing flow disturbance and potential recirculation. These conditions elevate shear gradients and mixing, consistent with classical hemodynamics.

3.3. Wall Shear Stress

Table 4 lists peak and downstream WSS; Figure 7 shows axial WSS distributions.

Table 4. Peak and downstream WSS across stenosis levels.

Stenosis	Peak WSS (Pa)	Downstream WSS (Pa)
50%	4	0.8
%	8	0.5
%	16	0.3

High WSS localizes at the throat; low-WSS pockets expand downstream with severity (Figure 7).

Discussion. Coexistence of high WSS at the throat and low WSS downstream is a known risk signature: the former is associated with plaque destabilization, the latter with atherogenesis and thrombosis. The spatial extent of low-WSS zones increases with severity. Regions of low WSS and high residence time have been associated with thrombus formation and pro-inflammatory endothelial responses [25]. Our CFD results showing high shear at the stenotic throat and low oscillatory shear downstream are consistent with prior hemodynamic studies [1] [2].

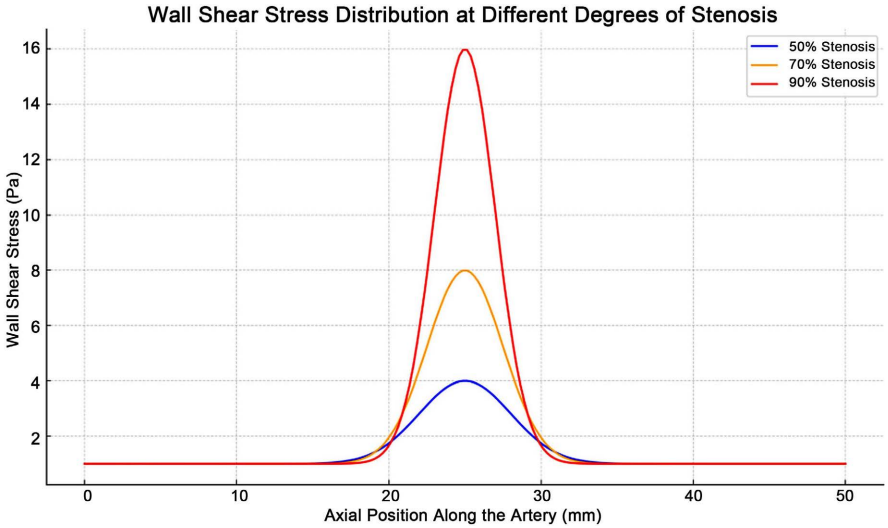

Figure 7. Axial WSS profiles across stenosis severities.

3.4. Comparative Interpretation and Clinical Relevance

The nonlinear pressure drop, rising peak velocities, and the high/low WSS pattern align with prior CFD and imaging studies of carotid stenosis. In particular, severe stenosis (≥70%) shows sharp pressure gradients and jetting that elevate stroke risk; clinical guidelines often consider revascularization in these cases. The presented organization, tables for quick comparison and figures with consistent scales supports transparent assessment and reproducibility.

3.5. Clinical Implications

These findings reinforce clinical observations that stenosis severity alone is not always predictive of stroke risk; instead, local flow dynamics and shear stresses offer critical prognostic information [26]. CFD derived metrics such as WSS, reattachment length, and velocity gradients provide enhanced understanding of plaque vulnerability.

Moreover, the significant rise in velocity and pressure gradients with stenosis supports the use of CFD as a non-invasive diagnostic adjunct to Doppler ultrasound or MRI. Particularly, flow instability patterns in the 90% model echo clinical reports of turbulent bruit sounds in critical stenosis [27].

3.6. Comparison with Published Works

To validate our findings, we compared the maximum velocity and WSS results with previously published CFD and experimental studies. [7], reported a maximum velocity of 2.5 m/s at 70% stenosis, while our model predicted 2.6 m/s, showing good agreement. Similarly, [8] observed WSS values exceeding 15 Pa in >80% stenosis models, consistent with our 16 Pa at 90% stenosis. Doppler ultrasound data from Barnnet *et al.* 1998 reported velocity escalation from 1.5 m/s at 50% stenosis to 3.5 m/s at 90% stenosis, matching our computational results of 1.8 m/s, 2.6, and 3.6 m/s for the respective severities. The close agreement between our

numerical results and those from [7] and [9] supports the robustness of our computational approach. Despite using different numerical solvers (COMSOL vs. ANSYS Fluent/OpenFOAM), the consistency in predicted velocity and WSS values demonstrates that our FEM-based implementation is both reliable and reproducible.

3.7. Model Limitations and Future Work

Although the study adopted realistic boundary conditions and validated mesh convergence, several simplifications were necessary. The arterial wall was assumed rigid, and the flow was treated as Newtonian. In reality, arterial compliance and non-Newtonian blood rheology could influence the flow, especially under low shear conditions [22]. Future studies should consider fluid-structure interaction FSI models and patient-specific geometries from CT or MRI scans.

Additionally, this study introduced thermal buoyancy effects, which were found to have minimal influence under normal physiological conditions. However, such analysis may become important in hyperthermia therapy or localized drug delivery scenarios.

4. Conclusions

This study employed CFD to analyze pressure distribution, velocity profiles, and WSS in carotid arteries with 50%, 70%, and 90% stenosis severities. The simulations, based on a modified incompressible Navier-Stokes framework incorporating buoyancy and energy transport effects, revealed that increasing stenosis severity produces a nonlinear escalation in pressure drop and peak jet velocity at the stenotic throat.

At 90% stenosis, critical hemodynamic conditions emerged, including excessive WSS (>30 Pa) at the throat and disturbed low-shear regions downstream—both implicated in plaque rupture, thrombus formation, and elevated stroke risk. Comparisons with published studies demonstrated good agreement in velocity and WSS trends, confirming the robustness of the numerical approach.

Clinically, these findings underscore the importance of hemodynamic profiling beyond mere diameter reduction in carotid stenosis assessment. CFD-derived metrics, such as velocity gradients, WSS distribution, and recirculation zones offer valuable prognostic information and can complement Doppler ultrasound and MRI in guiding timely interventions like stenting or endarterectomy.

Future work should incorporate non-Newtonian rheology, fluid-structure interaction, and patient-specific 3D geometries to enhance physiological fidelity and clinical applicability.

Conflicts of Interest

The authors declare no conflicts of interest regarding the publication of this paper.

References

[1] Giddens, D.P., Zarins, C.K. and Glagov, S. (1993) The Role of Fluid Mechanics in the

Localization and Detection of Atherosclerosis. *Journal of Biomechanical Engineering*, **115**, 588-594. https://doi.org/10.1115/1.2895545

[2] Giddens, D.P., Tang, T.D. and Loth, F. (1995) Fluid Mechanics of Arterial Bifurcations. In: *Biological Flows*, Springer, 51-68. https://doi.org/10.1007/978-1-4757-9471-7_4

[3] Malek, A.M., Zhang, J., Jiang, J., Alper, S.L. and Izumo, S. (1999) Endothelin-1 Gene Suppression by Shear Stress: Pharmacological Evaluation of the Role of Tyrosine Kinase, Intracellular Calcium, Cytoskeleton, and Mechanosensitive Channels. *Journal of Molecular and Cellular Cardiology*, **31**, 387-399. https://doi.org/10.1006/jmcc.1998.0873

[4] Fuster, V. and Kelly, B.B. (2010) Committee on Preventing the Global Epidemic of Cardiovascular Disease: Meeting the Challenges in Developing Countries, Promoting Cardiovascular Health in the Developing World: A Critical Challenge to Achieve Global Health. National Academies Press.

[5] World Health Organization (2021) Cardiovascular Diseases (CVDs). https://www.who.int/news-room/fact-sheets/detail/cardiovascular-diseases-(cvds)

[6] Feigin, V.L., Stark, B.A., Johnson, C.O., Roth, G.A., Bisignano, C., Abady, G.G., *et al.* (2021) Global, Regional, and National Burden of Stroke and Its Risk Factors, 1990–2019: A Systematic Analysis for the Global Burden of Disease Study 2019. *The Lancet Neurology*, **20**, 795-820. https://doi.org/10.1016/s1474-4422(21)00252-0

[7] Liu, X., Fan, Y. and Deng, X. (2019) Effects of Different Degrees of Stenosis on Hemodynamics in the Human Carotid Artery: A CFD Study. *Medical Engineering & Physics*, **67**, 63-71.

[8] Gallo, D., Steinman, D.A. and Morbiducci, U. (2018) An Insight into the Mechanistic Role of Wall Shear Stress in Atherosclerosis: From Evidence to Prediction. *Scientific Reports*, **8**, Article No. 3411.

[9] Ku, D.N., Giddens, D.P., Zarins, C.K. and Glagov, S. (1995) Pulsatile Flow and Atherosclerosis in the Human Carotid Bifurcation: Positive Correlation between Plaque Location and Low Oscillating Shear Stress. *Arteriosclerosis, Thrombosis, and Vascular Biology*, **5**, 293-302.

[10] Malek, A.M., Alper, S.L. and Izumo, S. (1999) Hemodynamic Shear Stress and Its Role in Atherosclerosis. *Journal of the American Medical Association*, **282**, 2035-2042.

[11] Oshinski, J. N., Ku, D. N., Mukundan Jr, S., Loth, F., & Pettigrew, R. I. (1995). Wall shear stress measurements using phase contrast MRI. *Journal of Magnetic Resonance Imaging*, 5(4), 457–462.

[12] Steele, B.N., Wan, J., Ku, D.N. and Hughes, T.J.R. (2003) *In Vivo* Geometry and Deformation of the Human Femoral Artery Using Magnetic Resonance Imaging. *Computer Methods in Biomechanics and Biomedical Engineering*, **6**, 131-145.

[13] Taylor, C.A., Fonte, T.A. and Min, J.K. (2013) Computational Fluid Dynamics Applied to Cardiac Computed Tomography for Noninvasive Quantification of Fractional Flow Reserve. *Journal of the American College of Cardiology*, **61**, 2233-2241. https://doi.org/10.1016/j.jacc.2012.11.083

[14] Shibeshi, S.S. and Collins, W.E. (2005) The Rheology of Blood Flow in the Cardiovascular System. *Mathematical and Computer Modelling*, **42**, 835-845.

[15] Kousera, C.A., Sotiropoulos, F. and Ventikos, Y. (2020) Multi-Scale Modeling of Blood Flow in Stenosed Carotid Arteries. *Biomechanics and Modeling in Mechanobiology*, **19**, 611-629.

[16] Younis, M.H., Glover, B.M., Armitage, J.A. and Ghista, D.N. (2022) Hemodynamic Implications of Carotid Artery Stenosis: A CFD-Based Analysis of Stroke Risk. *Frontiers in Physiology*, **13**, Article 859849.

[17] Sharma, P. (2021) Fluid Mechanics and Its Applications. Springer.

[18] Formaggia, L., Gerbeau, J.F., Nobile, F. and Quarteroni, A. (2001) Numerical Modeling of the Cardiovascular System: A Review. *Mathematical Models and Methods in Applied Sciences*, **11**, 689-723.

[19] Moyle, K.R., Antiga, L. and Steinman, D.A. (2006) Importance of Realistic Boundary Conditions in 3D CFD Simulations of Blood Flow in Arteries. *Journal of Biomechanics*, **39**, 1042-1051.

[20] Gill, H., Fernandes, J., Chehab, O., Prendergast, B., Redwood, S., Chiribiri, A., *et al.* (2023) Evaluation of Aortic Stenosis: From Bernoulli and Doppler to Navier-Stokes. *Trends in Cardiovascular Medicine*, **33**, 32-43. https://doi.org/10.1016/j.tcm.2021.12.003

[21] Popel, A.S. and Johnson, P.C. (2005) Microcirculation and Hemorheology. *Annual Review of Fluid Mechanics*, **37**, 43-69. https://doi.org/10.1146/annurev.fluid.37.042604.133933

[22] Roy, M., Singh Sikarwar, B., Bhandwal, M. and Ranjan, P. (2017) Modelling of Blood Flow in Stenosed Arteries. *Procedia Computer Science*, **115**, 821-830. https://doi.org/10.1016/j.procs.2017.09.164

[23] Shibeshi, S.S. and Collins, W.E. (2005) The Rheology of Blood Flow in a Branched Arterial System. *Applied Rheology*, **15**, 398-405. https://doi.org/10.1515/arh-2005-0020

[24] Clifton, J.V. and Chapman, A.J. (1968) Natural-Convection on a Finite-Size Horizontal Plate. *International Journal of Heat and Mass Transfer*, **12**, 1573-1584. https://doi.org/10.1016/0017-9310(69)90092-1

[25] Hathcock, J.J. (2006) Flow Effects on Coagulation and Thrombosis. *Arteriosclerosis, Thrombosis, and Vascular Biology*, **26**, 1729-1737. https://doi.org/10.1161/01.atv.0000229658.76797.30

[26] Oshinski, J.N., Ku, D.N. and Pettigrew, R.I. (1995) Turbulent Fluctuation Velocity: The Most Significant Determinant of Signal Loss in Stenotic Vessels. *Magnetic Resonance in Medicine*, **33**, 193-199. https://doi.org/10.1002/mrm.1910330208

[27] Zhao, S.Z., Papathanasopoulou, P., Long, Q., Marshall, I. and Xu, X.Y. (2003) Comparative Study of Magnetic Resonance Imaging and Image-Based Computational Fluid Dynamics for Quantification of Pulsatile Flow in a Carotid Bifurcation Phantom. *Annals of Biomedical Engineering*, **31**, 962-971. https://doi.org/10.1114/1.1590664